J. Fluid Mech. (2008), *vol.* 617, *pp.* 87–106.
doi:10.1017/S0022112008003753 Printed in the United Kingdom

Solidification of free liquid films

ANTHONY M. ANDERSON AND STEPHEN H. DAVIS

Department of Engineering Sciences and Applied Mathematics, McCormick School of Engineering and Applied Science, Northwestern University, Evanston, IL 60208, USA

(Received 29 February 2008 and in revised form 22 July 2008)

We examine steady longitudinal freezing of a two-dimensional single-component free liquid film. In the liquid, there are thermocapillary and volume-change flows as a result of temperature gradients along the film and density change upon solidification. We examine these flows, heat transfer, and interfacial shapes using an asymptotic analysis which is valid for thin films with small aspect ratios. These solutions depend sensitively on contact conditions at the tri-junctions. In particular, when the sum of the angles formed in the solid and liquid phases falls below a critical value, the existence of steady solutions is lost and the liquid film cannot be continuous, suggesting breakage of the film owing to freezing. The solutions are relevant to the freezing of foams of metals or ceramics, materials unaffected by surface active agents.

1. Introduction

Modelling solidification of a free liquid film requires formulating several free-boundary problems. Deformable interfaces separate the liquid phase from a passive gas phase, a moving solidification front separates the solid and liquid phases, and triple points (tri-junctions) are present where all three phases meet. The location of these boundaries must be determined as part of the solution and, in fact, are themselves active sources of heat and fluid flows. For instance, latent heat is released at the solidification front as it advances through the liquid phase. In addition, the liquid typically contracts (or expands) upon solidification. When this occurs, the solid–liquid interface acts as a fluid sink (or source) that drives a bulk volume-change flow in the liquid phase towards (or away from) the freezing front to conserve mass. Furthermore, longitudinal temperature gradients in the liquid film result in non-uniform surface tension at the gas–liquid interface. These interfacial stresses are transferred by viscosity to the bulk, resulting in a thermocapillary flow throughout the melt.

Consider a two-dimensional free liquid film, symmetric about its centreline, which is longitudinally frozen by pulling it through a heat exchanger with high and low temperatures that bracket the melting temperature. This unidirectional solidification set-up is illustrated in figure 1. We concern ourselves solely with the solidification of single component melts. In principle, by maintaining a fixed pulling speed, a steady state is eventually reached. Herein, we describe this steady configuration.

During the solidification of metallic foams, the thin liquid bridges (lamellae) separating adjacent gas bubbles are frozen. When this process is carried out successfully, a light-weight porous solid is produced which exhibits a high ratio of rigidity to specific weight and excellent energy absorption on impact. These are desirable properties in a number of applications, particularly those in the automotive and aerospace industries (see Banhart 2001; Weaire & Hutzler 2000). In aqueous

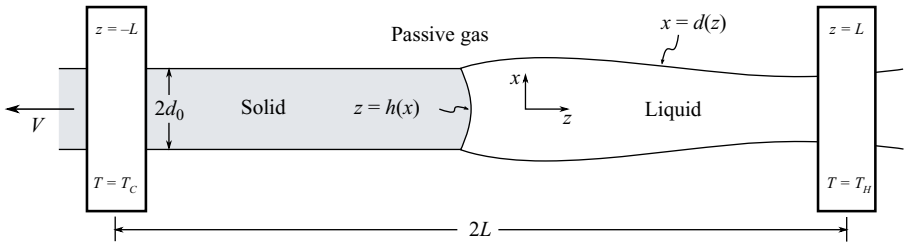

FIGURE 1. The free liquid film is frozen longitudinally by pulling it through a heat exchanger with high and low temperatures bracketing the melting temperature.

foams, surfactant is injected to immobilize the gas–liquid interfaces and stabilize the foam. In fact, the study of aqueous foams reduces to that of surfactant transport. In metals, there is no surfactant available, and so a principal difficulty in solidifying them comes from rapid coarsening ahead of the freezing front, which is the result of film rupture followed by coalescence of the adjacent gas bubbles. Film rupture can be measured in milliseconds for metals (Banhart *et al.* 2001). A detailed study of the microflows in individual lamellae is necessary for the prediction of thinning rates and rupture times, which ultimately set the time scales for coarsening. Such a study was given by Breward & Howell (2002) and extended by Brush & Davis (2005) for lamellae under isothermal conditions, but the effects of freezing have not yet been considered.

The set-up shown in figure 1 idealizes the solidification of a foam lamella. In particular, for metallic foams with low liquid fractions, the lamellar junctions (Plateau borders) will be relatively small. Consequently, it is reasonable to expect a uniform quasi-steady temperature in the Plateau borders. A single lamella which is being frozen is then a film between hot and cold regions. The results presented here are therefore particularly relevant to the solidification of metallic foams.

This method for freezing liquid films also shares many characteristics with containerless solidification in industry. In meniscus-defined systems, such as float-zone and Czochralski systems, among others (for example, see Brown 1988), the melt is contained by its own surface tension. In the float-zone technique, a solid polycrystalline rod is fed past a heating coil where it melts and then resolidifies into a single crystal. The liquid melt region forms a meniscus which bridges the two solid phases. Here, thermocapillary convection in the melt has received much attention since it has important implications on the overall size and quality of the crystal produced (for example, see Kuhlmann 1999). Extensive literature is devoted to describing these fluid dynamics using simplified systems such as half-zone and full-zone models in which the processes of freezing and melting are not considered. Further, floating zones have circular cross-sections that may be susceptible to Rayleigh breakup.

Our analysis of the freezing film shown in figure 1 takes advantage of the small aspect ratio $A \equiv d_0/L$. There is previous work on steady thermocapillary flows induced by longitudinal temperature gradients in thin liquid layers (Levich 1962; Yih 1969; Sen & Davis 1982; Xu & Davis 1983; Sen 1986). The first rational asymptotic theory in the limit $A \to 0$ is given by Sen & Davis (1982). They treat a liquid layer in a shallow two-dimensional slot which has sidewalls held at different temperatures, and find steady solutions using an asymptotic matching procedure. In the core region, away from the sidewalls, the solutions have nearly parallel flow and a nearly flat gas–liquid interface. Boundary-layer corrections near the sidewalls, where the flow

turns over, are matched to the core flow. This approach was extended by Sen (1986) to allow for $O(1)$ deformations to the gas–liquid interface.

We extend this earlier work (Sen & Davis 1982; Sen 1986) to analyse the present problem. Note that here the fluid domain is bounded only at one end by the solid–liquid interface, and we must also address the phase transformation and accompanying volume-change flow. This adds new features to the analysis, since it involves solving the heat transfer problem across both the solid and liquid phases and simultaneously determining the location of the freezing front, which is *a priori* unknown. To this end, we obtain approximate solutions for the solid and liquid temperature profiles as well as for the fluid flow in the limit $A \to 0$. In deriving these solutions, we incorporate convection in the melt, latent heat, and deformations to the solid–liquid interface systematically within a consistent asymptotic framework.

2. Formulation

Let the distance between the two heat exchanger plates in figure 1 be given by $2L$. The freezing temperature of the melt lies between the temperatures T_H and T_C of the hot and cold plates, respectively. In principle, by maintaining a fixed pulling speed V, a steady state like the one shown can be reached in which a solid bar of uniform thickness $2d_0$ is produced. In this section, we first write down the conservation equations and boundary conditions which describe this steady-state configuration. This description will include thermocapillary and volume-change flows in the melt which are bounded by deformable gas–liquid and solid–liquid interfaces.

2.1. *Governing equations and boundary conditions*

In the frame of reference shown in figure 1, let x measure distance from the film centreline and z measure distance along the film. The liquid phase is assumed to be an incompressible Newtonian fluid governed by the following mass and momentum balances

$$\nabla \cdot \boldsymbol{v} = 0, \tag{2.1}$$

$$\rho_l(\boldsymbol{v} \cdot \nabla \boldsymbol{v} - V \boldsymbol{v}_z) = -\nabla p + \mu \nabla^2 \boldsymbol{v}, \tag{2.2}$$

where μ is the dynamic viscosity and ρ_l is the liquid density (subscripts on dependent variables denote partial differentiation). Here, $\boldsymbol{v} = (u, w)$ is the additional fluid motion arising from thermocapillary and volume-change effects. We have assumed that gravity is negligible, which is a good approximation when the film is thin and the distance between the plates is not too large. The steady temperature distributions in the solid (T^s) and liquid (T^l) phases are governed by the following heat balances

$$\boldsymbol{v} \cdot \nabla T^l - V T^l_z = \kappa_l \nabla^2 T^l \quad (z > h), \tag{2.3}$$

$$-V T^s_z = \kappa_s \nabla^2 T^s \quad (z < h), \tag{2.4}$$

where κ_l and κ_s are liquid and solid thermal diffusivities. We assume constant densities and thermal properties in the liquid and solid.

The film is symmetric about its centreline, and we consider only the region $x \geqslant 0$. This symmetry is ensured by the following boundary conditions at $x = 0$,

$$u = w_x = T^l_x = T^s_x = 0. \tag{2.5}$$

At the gas–liquid interface, $x = d(z)$, there is a kinematic condition

$$(\boldsymbol{v} - V \boldsymbol{k}) \cdot \boldsymbol{n}_{gl} = 0 \tag{2.6}$$

and stress balance

$$\boldsymbol{S}\cdot\boldsymbol{n}_{gl} = -\sigma(T)\mathscr{K}(d)\,\boldsymbol{n}_{gl} + \frac{\mathrm{d}\sigma}{\mathrm{d}T}(\nabla T\cdot\boldsymbol{t}_{gl})\boldsymbol{t}_{gl}, \tag{2.7}$$

where $\boldsymbol{S} = -p\boldsymbol{I} + \mu[\nabla\boldsymbol{v} + (\nabla\boldsymbol{v})^T]$ is the stress tensor, $\boldsymbol{n}_{gl} = (1, -d_z)/\sqrt{1+d_z^2}$ is the unit normal vector to the gas–liquid interface pointing out of the liquid, $\boldsymbol{t}_{gl} = (d_z, 1)/\sqrt{1+d_z^2}$ is the unit tangent vector, $\boldsymbol{k} = (0, 1)$ is a unit vector in the z-direction, and $\mathscr{K}(d) = -d_{zz}(1+d_z^2)^{-3/2}$ is twice the mean curvature. The temperature dependence of the surface tension $\sigma(T)$ in (2.7) is specified through a linear equation of state,

$$\sigma(T) = \sigma_0 - \gamma\,(T - T_m)\,, \tag{2.8}$$

where σ_0 is the surface tension at the equilibrium melting temperature T_m. The normal stresses in (2.7) balance the Laplace pressure, $\sigma\mathscr{K}$, and the tangential stresses balance gradients in the surface tension as a result of temperature variations along the interface. We consider the case where $\gamma = -\,\mathrm{d}\sigma/\mathrm{d}T > 0$, which is the case for common liquids, so that the shear stress along the gas–liquid interface is directed from hot to cold. These stresses drive thermocapillary flow in the film.

The solid–liquid interface is the site of a phase transformation in which the liquid of density ρ_l changes to a solid of density ρ_s. A mass balance at $z = h(x)$ gives

$$\rho_l\,\boldsymbol{v}\cdot\boldsymbol{n}_{sl} = (\rho_l - \rho_s)\,V\boldsymbol{k}\cdot\boldsymbol{n}_{sl}, \tag{2.9}$$

where $\boldsymbol{n}_{sl} = (-h_x, 1)/\sqrt{1+h_x^2}$ is the unit normal pointing into the liquid. Since this interface is a rigid boundary, the following no-slip condition applies at $z = h(x)$ as well

$$\boldsymbol{v}\cdot\boldsymbol{t}_{sl} = 0, \tag{2.10}$$

where $\boldsymbol{t}_{sl} = (1, h_x)/\sqrt{1+h_x^2}$ is the unit tangent to the interface. From (2.9), we see that when $\rho_s = \rho_l$, the interface is impermeable to flow, but when $\rho_s \neq \rho_l$, it acts as a source ($\rho_s < \rho_l$) or sink ($\rho_s > \rho_l$) for flow with strength proportional to the solidification speed. This is the origin of volume-change flow in the film.

Thermal boundary conditions are specified next. We assume that the sides are insulated by the passive gas phase which requires the following no-flux conditions

$$\nabla T^l\cdot\boldsymbol{n}_{gl} = 0 \quad \text{at } x = d(z), \tag{2.11}$$

$$T_x^s = 0 \quad \text{at } x = d_0. \tag{2.12}$$

At the hot and cold plates, we prescribe the temperature

$$T^l = T_H \quad \text{at } z = L, \tag{2.13}$$

$$T^s = T_C \quad \text{at } z = -L, \tag{2.14}$$

implying perfect thermal contact between the film and the plates. When local equilibrium prevails at the solid–liquid interface, the temperature is continuous there. At $z = h(x)$, the thermodynamic freezing temperature for the deformable interface is given by the Gibbs–Thompson relation

$$T^l = T^s = T_m\left(1 - \frac{\hat{\gamma}}{L_v}\mathscr{K}(h)\right), \tag{2.15}$$

where $\mathscr{K}(h) = -h_{xx}(1+h_x^2)^{-3/2}$ is twice the mean curvature of the interface, $\hat{\gamma}$ is the interfacial surface energy, and L_v is the latent heat of fusion per unit volume of

solid. This relation states that a solid finger extending into the liquid will melt at temperatures below T_m owing to curvature. Also at $z = h(x)$, there is a heat balance which accounts for the continuous production of latent heat

$$(k_s \nabla T^s - k_l \nabla T^l) \cdot \boldsymbol{n}_{sl} = L_v V \boldsymbol{k} \cdot \boldsymbol{n}_{sl}, \tag{2.16}$$

where k_s and k_l are solid and liquid thermal conductivities.

2.2. *Lubrication scaling*

The disparate length scales d_0 and L motivate a lubrication-type scaling of the governing equations and boundary conditions. We introduce the following dimensionless (primed) quantities:

$$x = d_0 x', \quad z = L z', \quad d = d_0 d', \quad h = L h',$$

$$u = A w_\star u', \quad w = w_\star w', \quad p = (\mu w_\star / A d_0) p', \quad T = T_m + (T_H - T_C) T',$$

where $A = d_0/L$ is the aspect ratio of the film. The velocity scale $w_\star$ is determined from the relative strengths of the thermocapillary and volume-change flows. The characteristic velocity scale for thermocapillary flow is determined by examining the the tangential component of (2.7). Balancing viscous shear stresses and surface tension gradients leads to the velocity scale

$$w_{tc} = \frac{\gamma A (T_H - T_C)}{\mu}.$$

Similarly, the characteristic velocity scale for volume-change flow is determined by the interfacial mass balance (2.9). The velocity scale is proportional to the rate of volume change

$$w_{vc} = \frac{|\rho_l - \rho_s| V}{\rho_l}.$$

In § 4, we discuss the three cases $w_{vc} \gg w_{tc}$ $w_{vc} \ll w_{tc}$ and $w_{vc} \sim w_{tc}$.

This rescaling is now applied to the system (primes are dropped). By introducing a dimensionless streamfunction ψ, such that

$$\boldsymbol{v} - W^{-1} \boldsymbol{k} = (\psi_z, -\psi_x), \tag{2.17}$$

where $W = w_\star / V$, the continuity equation is satisfied automatically and both components of the momentum equation can be combined into a single equation in which the pressure is eliminated, yielding

$$\psi_{xxxx} + 2A^2 \psi_{xxzz} + A^4 \psi_{zzzz} = AWR[\psi_z(\psi_{xxx} + A^2 \psi_{xzz}) - \psi_x(\psi_{xxz} + A^2 \psi_{zzz})]. \tag{2.18}$$

Dimensionless equations for the liquid and solid temperatures take the form

$$T^l_{xx} + A^2 T^l_{zz} = AWP\left(\psi_z T^l_x - \psi_x T^l_z\right), \tag{2.19}$$

$$T^s_{xx} + A^2 T^s_{zz} = -AP\kappa^{-1} T^s_z. \tag{2.20}$$

Along the sides of the film, we have at $x = d(z)$ the scaled tangential stress balance

$$\left[4A^2 d_z \psi_{xz} - \left(1 - A^2 d_z^2\right)(\psi_{xx} - A^2 \psi_{zz})\right]\left(1 + A^2 d_z^2\right)^{-1} = -AM\left(d_z T^l_x + T^l_z\right)\left(1 + A^2 d_z^2\right)^{-1/2}, \tag{2.21}$$

and normal stress balance

$$-p + 2A^2\left[\left(1 - A^2 d_z^2\right)\psi_{xz} + d_z(\psi_{xx} - A^2\psi_{zz})\right]\left(1 + A^2 d_z^2\right)^{-1} = A^3 C^{-1} d_{zz}\left(1 - CMT^l\right)\left(1 + A^2 d_z^2\right)^{-3/2}, \quad (2.22)$$

as well as the no-flux conditions

$$T_x^l = A^2 d_z T_z^l \quad \text{at } x = d, \quad (2.23)$$

$$T_x^s = 0 \quad \text{at } x = 1. \quad (2.24)$$

The kinematic condition is equivalent to specifying the value of the streamfunction at $x = d(z)$, such that

$$\psi = \psi_w = -\int_0^{d(z)} (w - W^{-1})\,\mathrm{d}x, \quad (2.25)$$

since, for steady solutions, the total flow rate must be the same through every cross-section. At the film centreline, $x = 0$, the symmetry conditions are

$$\psi = \psi_{xx} = T_x^l = T_x^s = 0. \quad (2.26)$$

Dimensionless boundary conditions at $z = h(x)$ take the form

$$W\left(h_x\psi_z + \psi_x\right) = \rho, \quad (2.27)$$

$$W(h_x\psi_x - A^2\psi_z) = h_x, \quad (2.28)$$

$$T^l = T^s = A^{-1}\Gamma h_{xx}\left(1 + A^{-2}h_x^2\right)^{-3/2}, \quad (2.29)$$

$$\rho\kappa\left(A^2 T_z^s - h_x T_x^s\right) - \left(A^2 T_z^l - h_x T_x^l\right) = A\mathscr{L}, \quad (2.30)$$

which are derived from (2.9), (2.10), (2.15) and (2.16), respectively. Finally, at the hot and cold plates, we have

$$T^l = \theta_H \quad \text{at } z = 1, \quad (2.31)$$

$$T^s = \theta_C \quad \text{at } z = -1, \quad (2.32)$$

where $\theta_H = (T_H - T_m)/(T_H - T_C)$ and $\theta_C = (T_C - T_m)/(T_H - T_C)$ are the scaled plate temperatures. The dimensionless parameters that appear in the equations above are defined in table 1.

3. Matched asymptotic analysis

We are interested in films with small aspect ratios ($A \ll 1$). In this section, approximate asymptotic solutions are found in the limit $A \to 0$. In this limit, a regular perturbation is not uniformly valid: there exists a boundary-layer (inner) region of thickness $O(A)$ at the solid–liquid interface. On the one hand, thermocapillary flow driven from hot to cold must recirculate at the solid–liquid interface in order to conserve mass, causing an appreciable transverse flow. We follow Sen & Davis (1982), who treat these turnover flows as boundary-layer corrections matched to an outer (core) flow. On the other hand, because the solid–liquid interface is deformable in the present case, a boundary layer is, in general, necessary to satisfy the boundary conditions there. Of course, the size of these deformations cannot exceed $O(A)$, the thickness of the boundary layer.

Dimensionless parameter		Definition	Typical size (metallic foams)
A	aspect ratio	$\dfrac{d_0}{L}$	$\lesssim 10^{-1}$
W	speed ratio	$\dfrac{w_\star}{V}$	Arbitrary
κ	thermal diffusivity ratio	$\dfrac{\kappa_s}{\kappa_l}$	≈ 2
ρ	density ratio	$\dfrac{\rho_s}{\rho_l}$	≈ 1
R	Reynolds number	$\dfrac{d_0 \rho_l V}{\mu}$	$\lesssim 10^{-1}$
P	Péclet number	$\dfrac{d_0 V}{\kappa_l}$	$\lesssim 10^{-2}$
C	capillary number	$\dfrac{\mu w_\star}{\sigma_0}$	$\lesssim 10^{-2}$
M	Marangoni number	$\dfrac{\gamma(T_H - T_C)}{\mu w_\star}$	Arbitrary
$\mathscr{L}$	Stefan number	$\dfrac{d_0 L_v V}{k_l(T_H - T_C)}$	Arbitrary
Γ	surface energy number	$\dfrac{\hat{\gamma} T_m}{d_0 L_v (T_H - T_C)}$	$\lesssim 1$

TABLE 1. The dimensionless parameters appearing in (2.17)–(2.32) are defined. In the right-hand column, typical values for a metallic foam system are given in order to provide a point of reference for the developement of our model in § 3. In § 5, the primary assumptions of the model are discussed in the context of specific examples.

Below, matched asymptotic expansions are constructed in the inner and outer regions to form leading-order composite solutions which are valid over the entire domain. The asymptotic analysis is based on the following limits:

$$M = A^{-1}\bar{M}, \quad R = A\bar{R}, \quad P = A\bar{P}, \quad C = A^3\bar{C}, \quad \mathscr{L} = A\bar{L},$$

with $\bar{M}$, $\bar{R}$, $\bar{P}$, $\bar{C}$ and $\bar{L}$ all $O(1)$ as $A \to 0$. Parameters which are not listed above are assumed to be of unit order. The limit $M = A^{-1}\bar{M}$ is chosen to include thermocapillary effects in the leading-order balance. However, variations in surface tension are still small along the film since $CM = A^2\bar{C}\bar{M}$ requires that $\sigma_0 \gg \gamma(T_H - T_C)$. The limit $R = A\bar{R}$ holds for slow viscous flow, where inertial terms do not play a role in the leading approximation. The assumption $P = A\bar{P}$ represents a distinguished limit in the thermal problem. We show that, as a result of the no-flux conditions along the sides, pure conduction does not hold in this limit with convection entering from the net flow produced from volume change. Note that these choices for R and P correspond to Prandtl numbers, $Pr = P/R = \nu/\kappa_l$, of unit order. Prandtl numbers of different sizes are obtained using different limits for R and P. With the assumption $C = A^3\bar{C}$, the capillary pressure is expressed at leading order and, as Sen (1986) has pointed out, the gas–liquid interface may undergo $O(1)$ deformations. Lastly, we discuss the Stefan number limit $\mathscr{L} = A\bar{L}$ further when we introduce scalings and derive solutions for the inner region.

The prescription of contact conditions has important implications for the overall morphology of the deformable interfaces. We examine a situation in which the

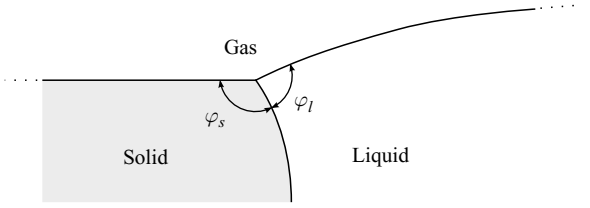

FIGURE 2. Close-up of the tri-junction region with angles φ_s and φ_l measured in the solid and liquid, respectively.

gas–liquid interface is pinned at a fixed location on the hot plate. This is realistic; however, choices which allow the interface to move freely along the hot plate may be more appropriate in specific situations (for example, the prescription of curvature at the hot plate coarsely models a lamella 'joined' with an adjacent Plateau border. See Breward & Howell (2002) and Brush & Davis (2005) for a more detailed model). At the tri-junctions, where the gas, liquid and solid phases meet, the contact conditions are illustrated in figure 2. The gas–solid and solid–liquid interfaces which form angle φ_s are allowed to be nearly perpendicular by taking $\varphi_s = \pi/2 + A\alpha$, with $\alpha = O(1)$ as $A \to 0$. For the intersection of the gas–liquid and solid–liquid interfaces, we consider liquid angles $\varphi_l = \pi/2 + A\beta$, with $\beta = O(1)$ as $A \to 0$. These choices for $\varphi_{s,l}$ are consistent with the small-slope analysis used here.

A few comments should be made about the prescription of contact conditions at the tri-junctions. Integrable point singularities in the pressure and stress fields are known to exist at tri-junctions, and they have been characterized according to wedge angle for thermocapillary (Anderson & Davis 1994*b*; Kuhlmann, Nienhuser & Rath 1999) and volume-change (Anderson & Davis 1994*a*) flows using a local analysis. In related problems (e.g. die-swell), it is known that when capillary forces enter the dominant balance at the tri-junction, infinite curvatures may arise (Schultz & Gervasio 1990). The extent of the region of large curvature decreases with decreasing capillary number (Salamon, Bornside & Armstrong 1995), indicating the singular nature of the limit $C \to 0$ near a contact line singularity (Anderson & Davis 1993). It follows that our prescription of the angles φ_s and φ_l is a macroscopic one – the microscopic angles may be different.

3.1. *Outer region*

Approximate solutions in the outer region are derived by introducing the following expansions

$$\psi \sim \psi_0 + A\psi_1, \quad p \sim p_0 + Ap_1, \quad T \sim T_0 + AT_1, \quad d \sim d_0 + Ad_1.$$

At leading order, we obtain the equations

$$T^l_{0xx} = 0, \quad T^s_{0xx} = 0, \quad \psi_{0xxxx} = 0, \tag{3.1}$$

with associated boundary conditions

$$x = 0 : T^l_{0x} = T^s_{0x} = 0, \tag{3.2}$$

$$\psi_0 = \psi_{0xx} = 0, \tag{3.3}$$

$$x = 1 : T^s_{0x} = 0, \tag{3.4}$$

$$x = d_0(z) : T^l_{0x} = 0, \tag{3.5}$$

$$\psi_0 = \psi_w, \ \ \psi_{0xx} = \bar{M}\left(d_{0z}T^l_{0x} + T^l_{0z}\right), \tag{3.6}$$

$$p_0 = -\bar{C}^{-1}d_{0zz}. \tag{3.7}$$

Equations (3.1*a*, *b*), (3.2), (3.4) and (3.5) admit x-independent solutions $T_0^l = T_0^l(z)$ and $T_0^s = T_0^s(z)$. In order for non-trivial solutions to exist, solvability conditions must be imposed at higher orders. Since $P = O(A)$, we see from (2.19) and (2.20) that these conditions are postponed to $O(A^2)$. First, we enforce solvability on the liquid side, where the $O(A^2)$ problem has the form

$$T_{2xx}^l = -T_{0zz}^l - W\bar{P}\psi_{0x}T_{0z}^l,$$

with boundary conditions

$$T_{2x}^l = 0 \qquad \text{at } x = 0,$$
$$T_{2x}^l = d_{0z}T_{0z}^l \quad \text{at } x = d_0(z).$$

In accordance with the Fredholm alternative, the following orthogonality condition must hold for solvability

$$\int_0^{d_0} \left(T_{0zz}^l + W\bar{P}\psi_{0x}T_{0z}^l\right) dx + d_{0z}T_{0z}^l = 0.$$

Using the boundary conditions (3.3*a*) and (3.6*a*), this is integrated to give

$$\left(d_0 T_{0z}^l\right)_z + W\bar{P}\psi_w T_{0z}^l = 0. \tag{3.8}$$

Proceeding similarly for the solid phase, solvability requires

$$T_{0zz}^s + \bar{P}\kappa^{-1}T_{0z}^s = 0. \tag{3.9}$$

Equations (3.8) and (3.9) must be supplemented with boundary conditions. From conditions at the hot and cold plates, (2.31) and (2.32), we have

$$T_0^l = \theta_H \quad \text{at } z = 1, \tag{3.10}$$
$$T_0^s = \theta_C \quad \text{at } z = -1. \tag{3.11}$$

We derive additional conditions from matching to the solutions in the inner region.

We now move on to solve the flow problem. The solution to (3.1*c*), (3.3) and (3.6) gives the leading-order streamfunction

$$\psi_0(x, z) = \frac{x\psi_w}{d_0} + \frac{\bar{M}}{6d_0}x\left(x^2 - d_0^2\right)T_{0z}^l. \tag{3.12}$$

From the $O(1)$ x-momentum balance, $p_{0x} = 0$, we conclude that the pressure is independent of x and given immediately by the normal stress condition (3.7),

$$p_0(z) = -\bar{C}^{-1}d_{0zz}. \tag{3.13}$$

Lastly, upon substituting p_0 and ψ_0 into the $O(1)$ z-momentum balance, $p_{0z} = -\psi_{0xxx}$, we have

$$d_0 d_{0zzz} = \bar{C}\bar{M}T_{0z}^l, \tag{3.14}$$

which is the equation for d_0. Equation (3.14) requires three boundary conditions. One comes from pinning the gas–liquid interface at a fixed position on the hot plate. For all the solutions presented here, we use

$$d_0 = 1 \quad \text{at } z = 1. \tag{3.15}$$

The remaining two conditions come from matching to the inner region.

3.2. *Inner region*

In the inner region, the appropriate stretching transformation is $z = A\tilde{z}$. In these variables, the equations for the streamfunction and temperature are

$$\nabla^4\psi = AW\bar{R}\left[\psi_{\tilde{z}}\left(\psi_{xxx} + \psi_{x\tilde{z}\tilde{z}}\right) - \psi_x\left(\psi_{xx\tilde{z}} + \psi_{\tilde{z}\tilde{z}\tilde{z}}\right)\right], \tag{3.16}$$

$$\nabla^2 T^l = AW\bar{P}\left(\psi_{\tilde{z}}T^l_x - \psi_x T^l_{\tilde{z}}\right), \tag{3.17}$$

$$\nabla^2 T^s = -A\bar{P}\kappa^{-1}T^s_{\tilde{z}}, \tag{3.18}$$

where $\nabla^2 = \partial_x^2 + \partial_{\tilde{z}}^2$ is the Laplacian operator. The boundary conditions transform as follows:

$$x = 0 : \psi = \psi_{xx} = T^l_x = T^s_x = 0, \tag{3.19}$$

$$x = 1 : T^s_x = 0, \tag{3.20}$$

$$x = d : T^l_x = d_{\tilde{z}}T^l_{\tilde{z}}, \tag{3.21}$$

$$\psi = \psi_w, \tag{3.22}$$

$$A\left[4d_{\tilde{z}}\psi_{x\tilde{z}} - \left(1 - d_{\tilde{z}}^2\right)\left(\psi_{xx} - \psi_{\tilde{z}\tilde{z}}\right)\right]\left(1 + d_{\tilde{z}}^2\right)^{-1} = -\bar{M}\left(d_{\tilde{z}}T^l_x + T^l_{\tilde{z}}\right)\left(1 + d_{\tilde{z}}^2\right)^{-1/2}, \tag{3.23}$$

$$A^2 p - 2A^3\left[\left(1 - d_{\tilde{z}}^2\right)\psi_{x\tilde{z}} + d_{\tilde{z}}\left(\psi_{xx} - \psi_{\tilde{z}\tilde{z}}\right)\right]\left(1 + d_{\tilde{z}}^2\right)^{-1} = -\bar{C}^{-1}d_{\tilde{z}\tilde{z}}\left(1 - A^2\bar{C}\bar{M}T^l\right)\left(1 + d_{\tilde{z}}^2\right)^{-1/2}, \tag{3.24}$$

$$\tilde{z} = \tilde{h} : W\left(\tilde{h}_x\psi_{\tilde{z}} + \psi_x\right) = \rho, \tag{3.25}$$

$$W\left(\psi_{\tilde{z}} - \tilde{h}_x\psi_x\right) = \tilde{h}_x, \tag{3.26}$$

$$T^l = T^s = \Gamma\tilde{h}_{xx}\left(1 + \tilde{h}_x^2\right)^{-3/2}, \tag{3.27}$$

$$\rho\kappa\left(T^s_{\tilde{z}} - \tilde{h}_x T^s_x\right) - \left(T^l_{\tilde{z}} - \tilde{h}_x T^l_x\right) = A\mathscr{L}. \tag{3.28}$$

Here, we have rescaled the height of the solid–liquid interface such that $h = A\tilde{h}$. Additionally, because we are setting $\varphi_s = \pi/2 + A\alpha$ and $\varphi_l = \pi/2 + A\beta$ (refer to figure 2), the contact conditions at the tri-junction have forms

$$d = 1, \quad d_{\tilde{z}} = A\left(\alpha + \beta\right), \quad \tilde{h}_x = -A\alpha. \tag{3.29}$$

Solutions are derived below by introducing the following inner expansions into the above equations and boundary conditions,

$$\psi \sim \tilde{\psi}_0 + A\tilde{\psi}_1, \quad p \sim \tilde{p}_0 + A\tilde{p}_1, \quad T \sim \tilde{T}_0 + A\tilde{T}_1, \quad d \sim \tilde{d}_0 + A\tilde{d}_1, \quad \tilde{h} \sim A\tilde{h}_1.$$

Note that deformations to the solid–liquid interface are assumed to be $O(A)$ in the inner region. We expect a planar interface at leading-order since it satisfies the contact conditions (i.e. setting $A = 0$ in (3.29*c*)) and is known to be stable. For convenience, we have chosen the leading-order position of the solid–liquid interface to be $\tilde{z} = 0$. Since this interface is a free boundary, this choice cannot be made arbitrarily. In the analysis below, we demonstrate that the latent heat balance results in an additional condition that must be enforced to ensure compatibility.

Equation (3.24) indicates that normal stresses on the gas–liquid interface result in an $O(A^2)$ perturbation. Consequently, since the curvature of the gas–liquid interface is zero up to $O(A)$, this yields

$$\tilde{d}_0 = 1, \quad \tilde{d}_1 = (\alpha + \beta)\tilde{z}, \tag{3.30}$$

which satisfy the contact conditions in (3.29*a*, *b*). When this result is matched to the outer solution, we obtain the following conditions

$$d_0 = 1, \quad d_{0z} = \alpha + \beta, \quad \text{at } z = 0, \tag{3.31}$$

which follows from Taylor expanding the outer solutions at $z = 0$ and comparing the result with (3.30). We see that the tri-junction conditions are simply transferred to the outer solution, providing the remaining conditions required in order to solve (3.14).

We move on to the $O(1)$ thermal problem. The solid and liquid temperatures satisfy the following leading-order equations

$$\nabla^2 \tilde{T}_0^s = 0, \quad \nabla^2 \tilde{T}_0^l = 0,$$

and boundary conditions

$$\begin{aligned} x = 0, 1: &\quad \tilde{T}_{0x}^s = \tilde{T}_{0x}^l = 0, \\ \tilde{z} = 0: &\quad \tilde{T}_0^s = \tilde{T}_0^l = 0. \end{aligned}$$

Further, matching to the outer region requires bounded solutions as $\tilde{z} \to \infty$. The only such solutions are the isothermal ones

$$\tilde{T}_0^s \equiv 0, \quad \tilde{T}_0^l \equiv 0. \tag{3.32}$$

Matching conditions for the outer solutions follow immediately:

$$T_0^s = T_0^l = 0 \quad \text{at } z = 0. \tag{3.33}$$

These provide the remaining conditions required in order to solve (3.8) and (3.9) for the temperature profiles in the outer regions. Note that in order to have isothermal solutions at leading order, we must take $\mathscr{L} = o(1)$ in the heat balance equation (3.28) as we have already done.

Before the leading-order flow problem can be solved in the inner region, it is necessary to determine the $O(A)$ temperature field to compute the thermocapillary stresses on the gas–liquid interface in (3.23). In the course of solving for temperature, we also obtain the $O(A)$ deformations to the solid–liquid interface. The $O(A)$ thermal problem involves the following equations

$$\nabla^2 \tilde{T}_1^s = 0, \quad \nabla^2 \tilde{T}_1^l = 0,$$

with boundary and contact conditions

$$\begin{aligned} x = 0: &\ \tilde{T}_{1x}^{s,l} = 0, && \tilde{h}_{1x} = 0, \\ x = 1: &\ \tilde{T}_{1x}^{s,l} = 0, && \tilde{h}_{1x} = -\alpha, \\ \tilde{z} = 0: &\ \tilde{T}_1^{s,l} = \Gamma \tilde{h}_{1xx}, && \rho\kappa \tilde{T}_{1\tilde{z}}^s - \tilde{T}_{1\tilde{z}}^l = \bar{L}. \end{aligned}$$

Here we have used the assumption $\mathscr{L} = A\bar{L}$, which was introduced ealier. In addition, there are matching conditions with the outer solution,

$$\tilde{T}_1^{s,l} \sim T_1^{s,l}\big|_{z=0} + \tilde{z}\, T_{0z}^{s,l}\big|_{z=0} \quad \text{as } \tilde{z} \to \infty.$$

Consider the following parabolic profile for the shape of the solid–liquid interface

$$\tilde{h}_1 = \tilde{H} - \tfrac{1}{2}\alpha x^2, \tag{3.34}$$

where $\tilde{H}$ is a constant. This profile is consistent with the contact conditions and has constant (linearized) curvature, leading to an isothermal melting temperature

at this order, specifically $\tilde{T}_1^{s,l} = -\alpha\Gamma$ at $\tilde{z}=0$. The corresponding solid and liquid temperature profiles are

$$\tilde{T}_1^{s,l} = -\alpha\Gamma + \left(T_{0z}^{s,l}\big|_{z=0}\right)\tilde{z}. \tag{3.35}$$

We have verified that (3.34) and (3.35) are the only possible solutions using cosine expansions for both $\tilde{h}_1$ and $\tilde{T}_1^{s,l}$. When (3.35) is substituted into the heat balance, we have

$$\left(\rho\kappa T_{0z}^{s} - T_{0z}^{l}\right)|_{z=0} = \bar{L}. \tag{3.36}$$

Recalling the remarks made earlier, the temperature field must be compatible with (3.36) in order to specify $\tilde{z}=0$ as the leading-order position of the solid–liquid interface. (The constant $\tilde{H}$ in (3.34) is determined from an analogous compatibility condition obtained from the $O(A^2)$ interfacial heat balance, not pursued here.) We deal with this compatibility condition in more detail in the next section.

Finally, we address the $O(1)$ flow problem. The convective terms in (3.16) do not contribute at leading order, so that

$$\nabla^4\tilde{\psi}_0 = 0. \tag{3.37}$$

The boundary conditions on $\tilde{\psi}_0$ are

$$x=0: \quad \tilde{\psi}_0 = \tilde{\psi}_{0xx} = 0 \tag{3.38}$$

$$x=1: \quad \tilde{\psi}_0 = \psi_w, \quad \tilde{\psi}_{0xx} = \bar{M}\left(T_{0z}^{l}\big|_{z=0}\right), \tag{3.39}$$

$$\tilde{z}=0: \quad \tilde{\psi}_0 = \rho W^{-1}x, \quad \tilde{\psi}_{0\tilde{z}} = 0, \tag{3.40}$$

and matching to the outer solution, (3.12), gives

$$\lim_{\tilde{z}\to 0}\tilde{\psi}_0 = \psi_w x + \tfrac{1}{6}\bar{M}\left(T_{0z}^{l}\big|_{z=0}\right)(x^2-1)x. \tag{3.41}$$

The boundary condition (3.40*a*) was derived from the mass balance (3.25) at the solid–liquid interface and, in this form, it is clear that $\psi_w = \rho W^{-1}$. The system, (3.37)–(3.41), can be solved using the following sine expansion

$$\tilde{\psi}_0 - \psi_w x - \frac{\bar{M}}{6}\left(T_{0z}^{l}\big|_{z=0}\right)(x^2-1)x = \sum_{n=1}^{\infty}\Psi_n(\tilde{z})\sin(n\pi x), \tag{3.42}$$

where we have introduced a particular solution to homogenize the boundary conditions in (3.38) and (3.39). When the system is transformed under this expansion, the coefficients $\Psi_n(\tilde{z})$ are found to satisfy

$$(D^2 - n^2\pi^2)^2\Psi_n(\tilde{z}) = 0,$$

with boundary conditions at $\tilde{z}=0$

$$\Psi_n = -\frac{2\bar{M}(-1)^n}{n^3\pi^3}T_{0z}^{l}|_{z=0}, \quad D\Psi_n = 0,$$

and with $\Psi_n \to 0$ as $\tilde{z}\to\infty$, where $D \equiv \mathrm{d}/\mathrm{d}\tilde{z}$. It follows that

$$\Psi_n(\tilde{z}) = -\frac{2\bar{M}(-1)^n T_{0z}^{l}|_{z=0}}{n^3\pi^3}\left(1 + n\pi\tilde{z}\right)\mathrm{e}^{-n\pi\tilde{z}}. \tag{3.43}$$

We can now write down a leading-order composite streamfunction

$$\psi_c \sim \psi_0 + \tilde{\psi}_0 - \psi_w x - \frac{\bar{M}}{6}\left(T^l_{0z}\big|_{z=0}\right)(x^2-1)x$$
$$= \left[\rho W^{-1} + \frac{\bar{M}}{6}\left(x^2 - d_0^2\right) T^l_{0z}\right]\frac{x}{d_0} + \sum_{n=1}^{\infty} \Psi_n(A^{-1}z)\sin(n\pi x), \quad (3.44)$$

which is valid throughout the liquid region.

4. Solutions

We begin with a summary of the results of the last section. The leading-order solid and liquid temperatures, $T_0^s(z)$ and $T_0^l(z)$, were found to satisfy

$$T^s_{0zz} + \bar{P}\kappa^{-1}T^s_{0z} = 0, \quad T_0^s(0) = 0, \quad T_0^s(-1) = \theta_C, \quad (4.1)$$
$$\left(d_0 T^l_{0z}\right)_z + \rho\bar{P}T^l_{0z} = 0, \quad T_0^l(0) = 0, \quad T_0^l(1) = \theta_H, \quad (4.2)$$

where we have made use of the substitution $\psi_w = \rho W^{-1}$ in (4.2*a*). Note that the temperature profile in the liquid is modified by the density ratio ρ since heat can be convected through the film by the volume-change flow. The leading-order position of the gas–liquid interface, $d_0(z)$, was found to satisfy

$$d_0 d_{0zzz} = \bar{C}\bar{M}T^l_{0z}, \quad d_0(0) = 1, \quad d_{0z}(0) = \alpha + \beta, \quad d_0(1) = 1. \quad (4.3)$$

We see here that the shape of the gas–liquid interface and the liquid temperature are tightly coupled. Once we have determined T_0^l and d_0 from the above boundary-value problems, the leading-order composite streamfunction is obtained from (3.44).

The solutions to (4.1)–(4.3) must be compatible with the leading-order heat balance at the solid–liquid interface given by (3.36). This constraint can be met, for example, by prescribing an appropriate temperature at the cold plate and fixing the values of all remaining parameters. The solution to (4.1) can be found readily,

$$T_0^s(z) = \theta_C\left(\frac{1 - \mathrm{e}^{-\bar{P}z/\kappa}}{1 - \mathrm{e}^{\bar{P}/\kappa}}\right). \quad (4.4)$$

Substituting this result into (3.36) and solving for θ_C gives

$$\theta_C = \frac{1}{\rho\bar{P}}\left(1 - \mathrm{e}^{\bar{P}/\kappa}\right)\left(\bar{L} + T^l_{0z}(0)\right), \quad (4.5)$$

which is the compatible temperature for the cold plate. This prescription was used to obtain the solid and liquid temperature profiles shown in figure 3. Here, and for all of the results that follow, we have used $\theta_H = 1$ for the hot-plate temperature.

We now examine flow patterns and deformations to the gas–liquid interface. Contours of the streamfunction ψ_c show the motion of the entire material volume which includes translation, whereas the contours of $\psi_c - W^{-1}x$ show only the additional fluid motion generated by thermocapillarity and volume change. In the figures that follow, we show both, since contours of the former are more conveniently observed in an experiment and contours of the latter allow us to examine the special features of the thermocapillary and volume-change effects.

First, consider the case with $\rho = 1$, where there is no change in density upon solidification. The gas–liquid interface and flow patterns for this case are plotted in figure 4 for two different contact angles, $\beta = 1$ and $\beta = -0.4$, with $\alpha = 0$ in both

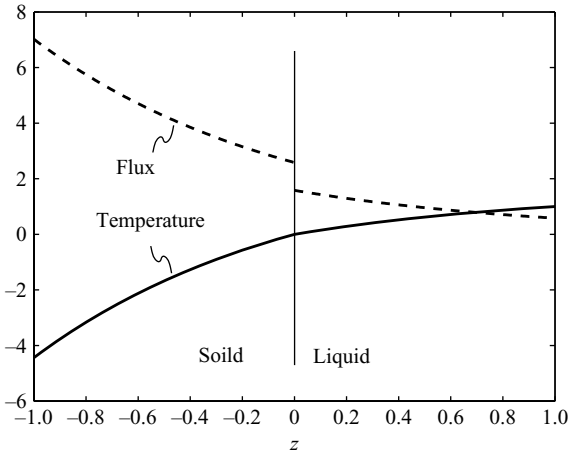

FIGURE 3. The leading-order temperature (——) and heat flux (- - -) are plotted for the solid and liquid phases ($\bar{M}=0$, $\rho=1$, $\bar{P}=1$, $\kappa=1$, $\alpha=\beta=0$). There is a jump of size $\bar{L}=1$ in the heat flux at the solid–liquid interface ($z=0$), verifying compatibility with the latent heat heat balance.

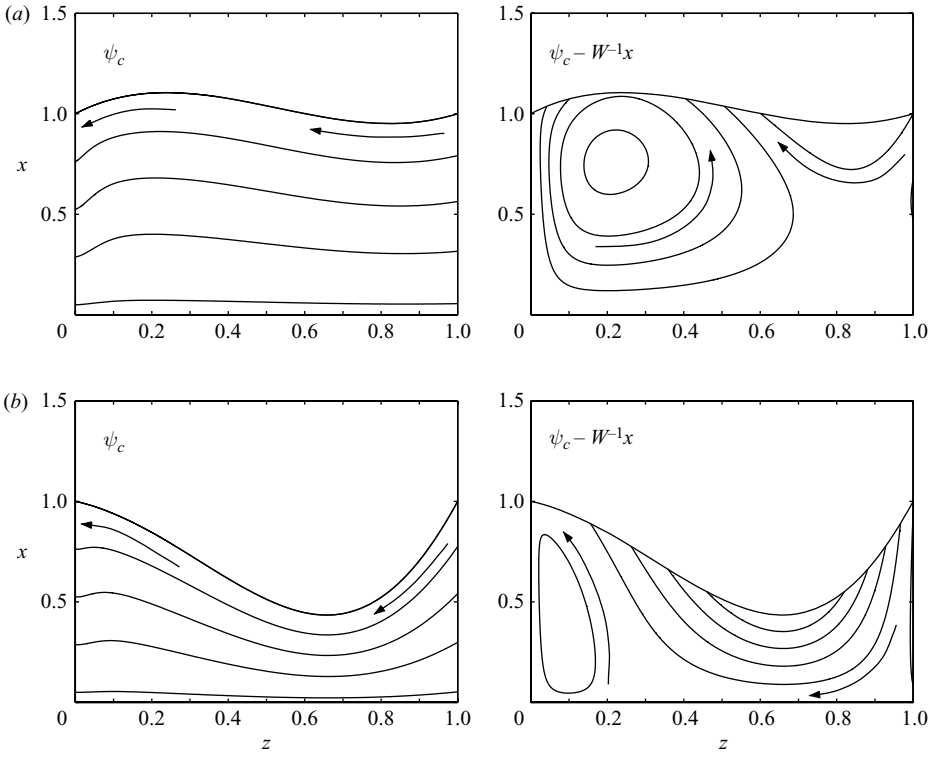

FIGURE 4. Deformations to the gas–liquid interface and flow patterns produced by thermocapillary flow for two contact conditions: (*a*) $\alpha=0$, $\beta=1$ and (*b*) $\alpha=0$, $\beta=-0.4$ ($W=1$, $\bar{P}=1$, $\bar{M}=1$, $\bar{C}=10$, $A=0.1$). There is no volume-change flow ($\rho=1$). The gas-liquid interface bulges near the solid–liquid interface because higher pressure is developed there by the recirculation of fluid. This is consistent with the solutions obtained by Sen & Davis (1982) and Sen (1986).

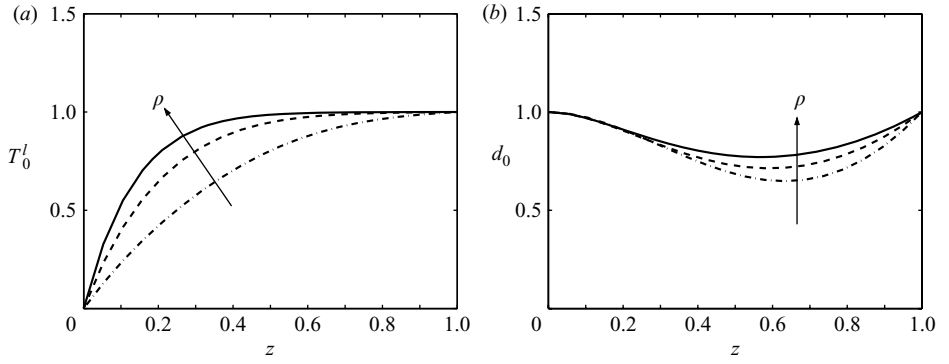

FIGURE 5. When $\bar{P} \neq 0$, volume-change flow convects heat towards ($\rho > 1$) or away from ($\rho < 1$) the solid–liquid interface which shifts the liquid temperature profile (a) and in turn deforms the gas-liquid interface (b). Letting $\bar{P} = 5$, $\bar{M} = 1$, $\bar{C} = 10$ and $\alpha = \beta = 0$, this effect is shown here for the three cases: $\rho = 0.5$ (dot-dash), $\rho = 1$ (dash), $\rho = 1.5$ (solid).

cases. Additionally, we have chosen the following parameter values: $W = 1$, $\bar{M} = 1$, $\bar{C} = 10$ and $\bar{P} = 1$. In both cases, the flows induced from thermocapillarity result in recirculation cells near the solidification front at $z = 0$. On account of the pronounced constriction of the film for $\beta = -0.4$, these recirculation cells are considerably more localized. If β is chosen as too negative, the film thickness vanishes between the solid–liquid interface and the hot plate and there is a loss of steady solutions. This indicates the importance of contact conditions in the solidification of liquid films. We come back to this point in the concluding section.

When we consider cases where $\rho \neq 1$, a portion of the flow is directed towards ($\rho > 1$) or away from ($\rho < 1$) the solidification front. In these cases, there is no direct contribution to the deformation of the gas–liquid interface through (4.3). However, volume change does alter the temperature profile because of convective heat flow and may therefore alter the morphology of the gas–liquid interface only when thermocapillarity is present. We see this effect in figure 5, where T_0^l and d_0 are compared for $\rho = 0.5$, 1 and 1.5. Additionally, we have chosen the following parameter values: $\bar{M} = 1$, $\bar{C} = 10$, $\bar{P} = 5$, $A = 0.1$ and $\alpha = \beta = 0$. We have shown in deriving (4.2) that convective heat flow enters the leading-order balance as a distinguished limit in which Prandtl numbers are of unit order, $Pr = \bar{P}/\bar{R} = O(1)$. For substances with $Pr = o(1)$ (e.g. metals), convection will not appear at leading order, and therefore the effect of volume change shown in figure 5 does not occur.

The relative magnitude of volume-change and thermocapillary flows is given by the ratio

$$\frac{w_{vc}}{w_{tc}} = \frac{|1-\rho|}{W\bar{M}}.$$

Through this relationship, the magnitude of w_{vc} decreases relative to w_{tc} by increasing W for fixed values of ρ and $\bar{M}$. In the sequence of plots in figures 6 and 7, flow patterns are shown for $W = 1$ (a), 5 (b) and 10 (c). We show expansion ($\rho = 0.5$) in figure 6 and contraction ($\rho = 1.5$) in figure 7. When $W = 1$, the contours of $\psi_c - W^{-1}x$ show no observable recirculation, and the dominant flow pattern is due to volume change. For $W = 5$ and $W = 10$, we see that in any given cross-section of the film, the portion that carries the volume-change flow shrinks as W is increased. Depending

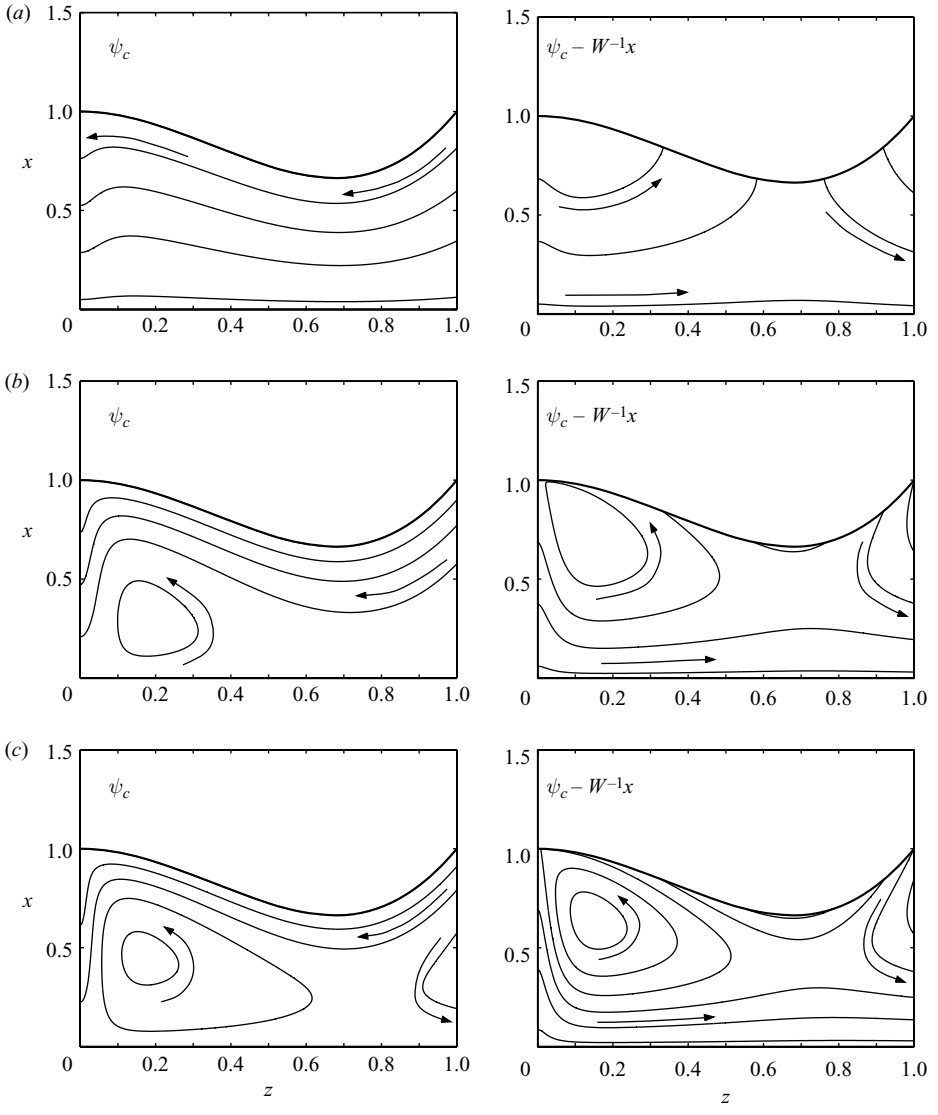

FIGURE 6. Flow patterns showing the superposition of thermocapillary and expansion ($\rho = 0.5$) flows. From top to bottom the strength of volume-change flow relative to thermocapillary flow is decreased: (*a*) $W = 1$, (*b*) 5, (*c*) 10. Referring to the flow patterns on the right, the expansion flow leaving the solid–liquid interface at $z = 0$ is swept below along the centreline by the recirculating portion of the flow.

on the value of ρ, this portion of the flow appears either along the film centreline ($\rho = 0.5$) or along the gas–liquid interface ($\rho = 1.5$). The remaining portion of the flow is simply recirculating fluid.

5. Discussion

In the present work, we have analysed steady longitudinal freezing of a two-dimensional single-component free liquid film, as the film is pulled at a constant speed through a heat exchanger which brackets the melting temperature. Thermocapillary

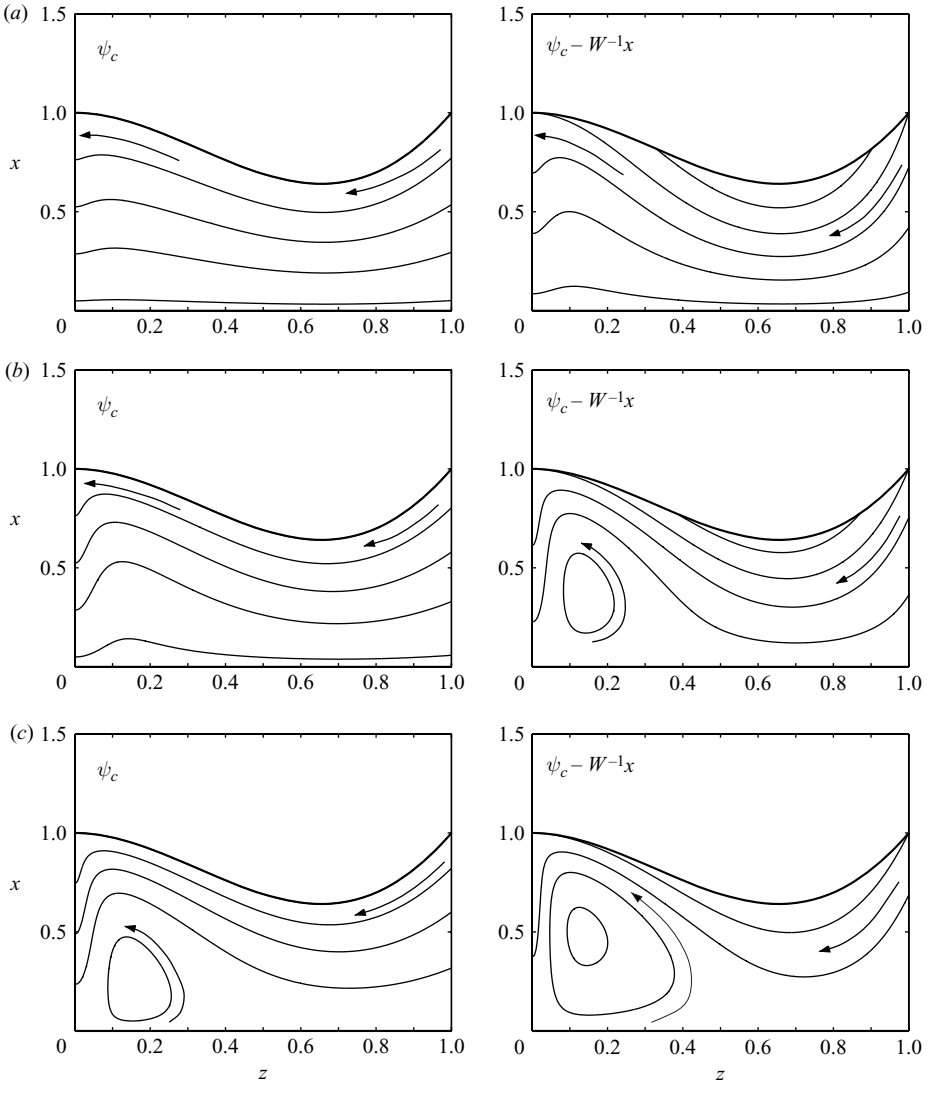

FIGURE 7. Flow patterns showing the superposition of thermocapillary and contraction ($\rho = 1.5$) flows. From top to bottom the strength of volume-change flow relative to thermocapillary flow is decreased: (*a*) $W = 1$, (*b*) 5, (*c*) 10. Referring to the flow patterns on the right-had side, the contraction flow is swept up along the gas–liquid interface before it is consumed at the solidification front ($z = 0$).

and volume-change fluid flows will occur in the melt as a result of temperature gradients along the film and density change upon solidification. Leading-order asymptotic solutions were derived in the limit of vanishing aspect ratio ($A \to 0$). These solutions describe fluid flows along with the thermal fields in the solid and liquid phases and deformations to the gas–liquid and solid–liquid interfaces. In table 2, we have included approximate non-dimensional parameter values for aluminium, silicon and water. The parameters listed are relevant to the discussion that follows.

In our treatment of the heat-transfer problem, we assume that no heat is lost to the surrounding gas phase. This assumption can be stated more precisely by

Material	T_m (K)	ρ	Pr	Bi	C	w_{vc}/w_{tc}
Aluminium	933.6	1.07	1.7×10^{-2}	1.1×10^{-5}	1.8×10^{-5}	(*a*) 0.07 (*b*) 0.70
Silicon	1683	0.91	1.2×10^{-2}	1.6×10^{-5}	1.5×10^{-5}	(*a*) 0.05 (*b*) 0.47
Water	273.2	0.92	9.7	1.7×10^{-3}	2.3×10^{-5}	(*a*) 0.08 (*b*) 0.83

TABLE 2. Here, we consider a film with dimensions $d_0 = 10^{-2}$ cm and $L = 1$ cm ($A = 10^{-2}$) which is pulled through the temperature gradient $(T_H - T_C)/L = 10$ K cm^{-1} at speeds (*a*) $V = 1$ cm s^{-1} and (*b*) 10 cm s^{-1}. Approximate parameter values are shown for aluminium, silicon and water, using physical constants valid at the melting points of each substance.

introducing a Biot number $Bi = h_g d_0 / k_{s,l}$, where h_g is the heat transfer coefficient for the gas phase, and $k_{s,l}$ is the heat conductivity of either the solid or liquid. The leading-order temperature profiles that we have obtained are valid for $Bi = o(A^2)$. We have calculated approximate Biot numbers for the materials in table 2 and see that this is a reasonable assumption when the surrounding air is still, which has $h_g \sim 10$ W m^{-2}K^{-1}. Sen & Davis (1982) treat the case with $Bi = O(1)$ but without phase transformation and show that the temperature distribution in the gas phase is inherited by the film. In some analyses of float zones, radiative heat losses were considered (see Rivas & Haya 1999), which could be important for materials with high melting points.

In our analysis of the fluid dynamics, inertia was neglected by considering Reynolds numbers $R = O(A)$. The fluid flow in excess of the translational speed of the front is thus given by a superposition of volume-change and thermocapillary flows with relative strengths $w_{vc}/w_{tc} = (|1 - \rho|/W)/(AM)$. Volume change produces plug flow towards ($\rho > 1$) or away ($\rho < 1$) from the solid–liquid interface and is expressed at leading order for $|1 - \rho|/W = O(1)$. In the case of thermocapillary flow, fluid is driven from hot to cold along the gas–liquid interface by surface tension gradients and recirculates as it approaches the solidification front. Turnover flow at the solid–liquid interface is treated as a boundary-layer correction which is matched to the outer flow. The resulting composite flow is expressed at leading order for Marangoni numbers $M = O(A^{-1})$.

Leading-order deformations to the gas–liquid interface occur with capillary numbers $C = O(A^3)$. The shape of the interface deviates from one of constant (linearized) curvature as a result of the thermocapillary flow, since a region of higher pressure at the solid–liquid interface is necessary to recirculate fluid there. Volume change, on the other hand, does not deflect the gas–liquid interface at leading order, since a pressure gradient is not required to drive the uniform flow produced. However, since volume change produces net flow through the film, it may convect heat. Such convection is negligible for metals which have Prandtl numbers $Pr \ll 1$. Convection would be observed at leading order for $Pr = O(1)$ with one example being water which expands upon solidification. As we have seen, the resulting shift in the liquid temperature profile has a relatively small effect on the deformation of the gas–liquid interface. This effect should not be overlooked when pulling speeds are large.

The shape of the solid–liquid and gas–liquid interfaces are also highly dependent on contact conditions. We have examined angles $\varphi_s = \pi/2 + A\alpha$ and $\varphi_l = \pi/2 + A\beta$ measured in the solid and liquid phases, respectively, with α and β that are $O(1)$ (refer to figure 2). With these contact conditions, we find that the gas–liquid interface intersects the solidification front with slope $\alpha + \beta$ and that the shape of the solidification front is a parabola with $O(A)$ amplitude, compared to the width of the

film, and with concavity given by the sign of $-\alpha$. The values of α and β therefore have a significant effect on the overall morphology of the solid–liquid and gas–liquid interfaces. Moreover, we observe that when the sum $\alpha + \beta$ is chosen sufficiently negative, the existence of steady solutions is lost. This suggests that the liquid bridge has broken owing to solidification, which is separate from film rupture resulting from a van der Waals instability.

The prescription of the contact conditions just described is a macroscopic one. It has already been commented in the beginning of § 3 that integrable stress singularities may be present at the tri-junctions which lead to large curvatures in the gas–liquid interface. This region of high curvature is localized to a microscopic region near the tri-junction for capillary numbers $C \to 0$. Consequently, a more careful prescription would consider the local dynamics at the tri-junctions which are responsible for 'selecting' the contact angle. This local analysis could be pursued numerically, similar to the work of Salamon *et al.* (1995) in the die-swell problem. The solutions presented in this work then serve as matching conditions 'at infinity' for the local flows calculated at the tri-junctions.

The steady solutions presented here form a basis for further study of the dynamics of freezing metallic foams. Of course, the foams are often three-dimensional, however, many of their essential features can be examined with a two-dimensional description which eliminates much of the geometrical complexity associated with the full three-dimensional problem. For instance, details of the microflows in individual lamellae are required for predicting lamellar thinning rates and rupture times, which ultimately set the timescales for coarsening. In this work, we have employed a two-dimensional model to examine the nature of the microflows produced by freezing. However, since lamellar thinning is an inherently unsteady and unstable process, further study will be required.

This research was supported by US National Science Foundation through the Research Training Group grant DMS-0636574.

REFERENCES

Anderson, D. M. & Davis, S. H. 1993 Two-fluid viscous flow in a corner. *J. Fluid Mech.* **257**, 1–31.

Anderson, D. M. & Davis, S. H. 1994*a* Fluid flow, heat transfer, and solidification near tri-junctions. *J. Crystal Growth* **142**, 245–252.

Anderson, D. M. & Davis, S. H. 1994*b* Local fluid and heat flow near contact lines. *J. Fluid Mech.* **268**, 231–265.

Banhart, J. 2001 Manufacture, characterisation, and application of cellular metals and metal foams. *Prog. Mat. Sci.* **46**, 559–632.

Banhart, J., Stanzick, H., Helfen, L. & Baumbach, T. 2001 Metal foam evolution studied by synchrotron radioscopy. *Appl. Phys. Lett.* **78**, 1152–1154.

Breward, C. J. W. & Howell, P. D. 2002 The drainage of a foam lemella. *J. Fluid Mech.* **458**, 379–406.

Brown, R. A. 1988 Theory of transport processes in single crystal growth from the melt. *AIChE J.* **34**, 881–911.

Brush, L. N. & Davis, S. H. 2005 A new law of thinning in foam dynamics. *J. Fluid Mech.* **534**, 227–236.

Kuhlmann, H. C. 1999 *Thermocapillary Convection in Models of Crystal Growth*. Springer.

Kuhlmann, H. C., Nienhuser, C. & Rath, H. J. 1999 The local flow in a wedge between a rigid wall and a surface of constant shear stress. *J. Engng Maths* **36**, 207–218.

Levich, V. G. 1962 *Physicochemical Hydrodynamics*. Prentice–Hall.

Rivas, D. & Haya, R. 1999 A conduction–radiation model for the floating-zone technique in monoellipsoidal mirror furnaces. *J. Crystal Growth* **206**, 230–240.

Salamon, T. R., Bornside, D. E. & Armstrong, R. C. 1995 The role of surface tension in the dominant balance in the die swell singularity. *Phys. Fluids* **7** (10), 2328–2344.

Schultz, W. W. & Gervasio, C. 1990 A study of the singularity in the die-swell problem. *Q. J. Mech. Appl Maths* **43**, 407–425.

Sen, A. K. 1986 Thermocapillary convection in a rectangular cavity with a deformable interface. *Phys. Fluids* **29** (11), 3881–3883.

Sen, A. K. & Davis, S. H. 1982 Steady thermocapillary flows in two-dimensional slots. *J. Fluid Mech.* **121**, 163–186.

Weaire, D. & Hutzler, S. 2000 *The Physics of Foams*. Oxford University Press.

Xu, J.-J. & Davis, S. H. 1983 Liquid bridges with thermocapillarity. *Phys. Fluids* **26** (10), 2880–2886.

Yih, C.-S. 1969 Three-dimensional motion of a liquid film induced by surface-tension variation or gravity. *Phys. Fluids* **12** (10), 1982.